

A reduced model for medial entorhinal cortex stellate cell: subthreshold oscillations, spiking and synchronization

Horacio G. Rotstein¹, Tim Oppermann²,
John A. White³, Nancy Kopell¹

¹ Department of Mathematics and Center for Biodynamics,
Boston University, Boston, MA, 02215, USA.

² Institute for Theoretical Biology,
Humboldt University Berlin, 10115 Berlin, Germany.

³ Department of Biomedical Engineering and Center for Biodynamics,
Boston University, Boston, MA, 02215, USA.

February 16, 2005

Abstract

Entorhinal cortex layer II stellate cells display subthreshold oscillations (STOs). We study a single compartment biophysical model of such cells which qualitatively reproduces these STOs. We argue that in the interspike interval (ISI) the seven-dimensional model can be reduced to a three-dimensional system of equations with well differentiated times scales. Using dynamical systems arguments we provide a mechanism for generations of STOS. This mechanism is based on the “canard structure”, in which relevant trajectories stay close to repelling manifolds for a significant interval of time. We also show that the transition from subthreshold oscillatory activity to spiking is controlled in the ISI by the same structure. The same mechanism is invoked to explain why noise increases the robustness of the STO

regime. Taking advantage of the reduction of the dimensionality of the full stellate cell system, we propose a generalized integrate-and-fire (GIF) model in which the ISI reduced system is supplemented with a threshold for spiking and a reset voltage. We show that the synchronization properties in networks made up of the GIF cells are similar to those of networks using the full stellate cell models.

Key words: theta rhythm; reduction of dimensions; Hopf bifurcation; canard phenomenon; generalized integrate-and-fire models.

1 Introduction

The flow of information from the neocortex to the hippocampus is orchestrated by the superficial cell layers (II and III) of the entorhinal cortex (EC). The large stellate cells (SCs) of Cajal constitute the most abundant principal cell type in layer II of the medial EC (MEC) and these neurons give rise to the perforant path, the main afferent fiber system to the hippocampus. *In vivo* electrophysiological investigations have shown that the MEC generates theta rhythm and that the firing of MEC layer II neurons is highly phase locked to theta field events. Many lines of evidence indicate that the theta rhythm is implicated in learning and memory processes, one of the main functions of the medial temporal lobe of which the EC is a crucial component. Importantly, *in vitro* electrophysiological studies have also established that the SCs develop low-amplitude (1-4 mV) rhythmic subthreshold membrane potential oscillations (STOs) at theta frequencies; when the membrane potential is set positive to threshold (about -50 mV), SCs fire action potentials at the peak of the STO but not necessarily at every STO's cycle (Dickson et al. 2000b). The coexistence of spiking and subthreshold (mixed-mode) oscillatory activity is a distinctive property of SCs *in vitro* and the firing of MEC layer II neurons has also been shown to skip theta cycles *in vivo*.

The persistent sodium (I_{Nap}) and h- (I_h) currents have been implicated in the pacemaking of single-cell rhythmicity at theta frequencies (Dickson et al. 2000a,b; Magistretti and Alonso 1999; Magistretti and Ragsdale 1999; Alonso and Llinás 1989; Alonso and Klink 1993; Klink and Alonso 1993, 1997; Fransén et al. 2004; Gillies et al. 2002; Rotstein et al. 2004) (see also references therein). The former constitutes a depolarization-activated fast inward current that provides the main drive for the depolarizing phase of the STOs. The latter, which is a hyperpolarization-activated non-inactivating

current with slow kinetics for both activation and deactivation, provides a delayed feedback effect that promotes resonance. (Note that the deactivation of an inward current is equivalent to the activation of an outward current). Theoretical studies, based on simulations of biophysical models, have shown that the interplay between I_h (with a fast and slow components) and I_{Nap} may be sufficient to account for the generation of membrane potential oscillations in layer II SCs (Dickson et al. 2000a,b; Fransén et al. 1998, 1999; White et al. 1995, 1998). However, the dynamic mechanism governing this interaction has not yet been explored.

The goal of this paper is to explain the dynamic mechanism governing the generation of subthreshold oscillations (STO), spikes and mixed-mode oscillatory (MMO) activity in a model of layer II SCs of the MEC which was introduced by Acker et al. (2003) to study the synchronization properties of SCs. We describe that model in Section 2. It incorporates a I_{Nap} and a two-component I_h (fast and slow) in addition to the standard sodium (I_{Na}), potassium (I_K) and leak (I_L) Hodgkin-Huxley (HH) currents.

We argue that, during the largest part of the interspike interval (ISI) regime, I_{Na} and I_K are inactive, leaving I_L , I_{Nap} , I_h (with its slow and fast components I_{h_f} and I_{h_s}) as the only active currents. In addition, the I_{Nap} gating variable p evolves on a much faster time scale than the rest of the remaining variables, so p is slaved to the voltage. Thus, the essential aspects of the dynamics of the SC during the ISI can be captured by a reduced three-dimensional system of differential equations, which describes the evolution of the voltage and the two I_h fast (r_f) and slow (r_s) gating variables.

At the heart of the mechanism of generation of STOs is a phenomenon associated with the geometry of invariant manifolds when there are multiple times scales. When an invariant manifold is unstable, in general trajectories starting near it quickly move away from it. However, if the invariant manifold is associated with slower motion, there are circumstances in which the trajectories starting adequately nearby can stay near the invariant manifold for a significant time. This phenomenon is known as a “canard structure” and is associated with a sudden increase in amplitude of the small oscillations to a large amplitude relaxation oscillation, for example, as some parameter is changed (Eckhaus 1983; Krupa and Szmolyan 2001; Dumortier and Roussarie 1996; Wechselberger 2004).

In this paper, we will not be concerned with large amplitude relaxation oscillation in the ISI regime, but with small amplitude oscillations, corresponding to STOs, that follow unstable invariant manifolds for a significant

part of the trajectory. The oscillations need not be limit cycles: they may spiral down to a fixed point, or spiral away from a fixed point. The paper concerns both these STOs and spikes, which belong to different trajectory “regimes”, in which different ionic currents are important and reduced equations describing the STOs are no longer valid. In our study of the STO’s we will use an initial condition that approximates the position of the trajectory after a spike, which is the relevant initial condition for the start of one or a series of STO’s.

The canard structure we have in mind is created by the 2D system of voltage and fast I_h gating variable. The slow component of I_h controls the STOs and governs the transition from the STOs to the spiking regimes. The spike provides a resetting mechanism that brings the system back to the ISI regime (where STOs occur).

One important and useful consequence of our results is that, if one is not interested in the spike details, the dynamics of the SC can be approximately described by the reduced three-dimensional system mentioned above, supplemented with a threshold for spiking and a reset voltage. We use this generalized integrate-and-fire (GIF) SC model to check the synchronization properties of networks of SCs (Acker et al. 2003; Jalicis et al. 2004) and to explain the effects of noise in enhancing the robustness of STOs (White et al. 1998).

2 Methods

The single compartment biophysical model we study here was introduced by Acker et al. (2003) and is based on measurements from layer II SCs of the medial entorhinal cortex (MEC) (White et al. 1995, 1998; Dickson et al. 2000b; Fransén et al. 2004). It has a persistent sodium (I_{Nap}) and a two-component (fast and slow) hyperpolarization-activated (I_h) currents in addition to the standard Hodgkin-Huxley sodium (I_{Na}), potassium (I_K) and leak (I_L) currents. The current-balance equation is

$$C \frac{dV}{dt} = I_{app} - I_{Na} - I_K - I_L - I_h - I_{Nap} \quad (1)$$

where V is the membrane potential (mV), C is the membrane capacitance ($\mu F/cm^2$), I_{app} is the applied bias (DC) current ($\mu A/cm^2$), $I_{Na} = G_{Na} m^3 h (V - E_{Na})$, $I_K = G_K n^4 (V - E_k)$, $I_L = G_L (V - E_L)$,

$I_{Nap} = G_p p (V - E_{Na})$, $I_h = G_h (0.65 r_f + 0.35 r_s) (V - E_h)$. G_X and E_X ($X = Na, K, L, p, h$) are the maximal conductances (mS/cm^2) and reversal potentials (mV) respectively. The units of time are $msec$. All the gating variables x ($x = m, h, n, p, r_f, r_s$) obey a first order differential equation of the following form:

$$\frac{dx}{dt} = \frac{x_\infty(V) - x}{\tau_x(V)}, \quad (2)$$

where

$$x_\infty(V) = \frac{\alpha_x(V)}{\alpha_x(V) + \beta_x(V)} \quad \text{and} \quad \tau_x(V) = \frac{1}{\alpha_x(V) + \beta_x(V)}. \quad (3)$$

The definitions of α_x and β_x for $x = m, h, n, p, r_f, r_s$ are given in the appendix and the corresponding graphs are shown in Fig. 1. The values of the parameters used by Acker et al. (2003) are $E_{Na} = 55$, $E_K = -90$, $E_L = -65$, $E_h = -20$, $G_{Na} = 52$, $G_K = 11$, $G_L = 0.5$, $G_p = 0.5$, $G_h = 1.5$ and $C = 1$.

Simulations were performed using the modified Euler method and a Runge-Kutta method of order IV (Burden and Faires 1980).

3 Results

3.1 Full model: Coexistence of subthreshold oscillations and spikes

In Fig. 2 we present simulation results for the full SC model for various values of I_{app} . The voltage traces are shown in the two top panels (note that the second panel is a blow-up of the top panel); the I_h and I_{Nap} traces are given in the two bottom panels. As the value of I_{app} increases, the spiking frequency also increases, while the number of STOs per ISI decreases and finally vanishes as shown in Fig. 2-d. In all simulations we have done we found that, for relevant initial conditions, voltage traces either display STOs and spikes, or decay to a fixed point in an oscillatory way. In most cases, STOs increase their amplitude as the SC trajectory approaches spiking.

Our results demonstrating the coexistence of STOs and spikes are consistent with experimental findings (Dickson et al. 2000b). However, the STOs

predicted using the deterministic full SC model are less robust than experimentally found; i.e., the ratio STO/spikes is larger in experiments than in simulations. In Section 3.4 we explain how noise is able to correct for this.

Note that, as experimentally found (Dickson et al. 2000a), I_{Nap} is at a minimum at the trough of a STO, and I_h reaches its maximum at the beginning of the depolarizing phase. As depolarization proceeds, I_{Nap} rapidly increases, boosting the depolarization initiated by I_h , which in itself causes the voltage trajectory to reverse to repolarization. Just after the peak of the oscillation, I_h reaches its minimum

3.2 A reduced SC model valid during the ISI

Here we argue that, during the ISI, I_{Na} and I_K are almost inactive, leaving I_{Nap} , I_h and I_L as the main active currents. We also show that $p \sim p_\infty(V)$, so the dynamics of the SC can be approximated by a three-dimensional system describing V , r_f and r_s . A more precise mathematical analysis of this will be given in a related work (Rotstein et al. 2005).

3.2.1 Reduced equations

Looking at the second panels in Fig. 2 we see that during most of the ISI the voltage is bounded between $-60 mV$ and $-50 mV$. In Figs. 1-e to -f, we see that for this interval of values of the voltage, τ_p , τ_m and τ_n are much smaller than τ_{r_f} , which we take as a reference time scale. In addition, from Fig. 1-d, $m_\infty \sim 0$ and $n_\infty^4 \sim 0$. Then $m \sim 0$, $I_{Na} \sim 0$, $I_K \sim 0$ and $p \sim p_\infty(v)$. Thus, we get the following system of equations to approximately describe the dynamics of the SC model during the ISI:

$$C \frac{dV}{dt} = I_{app} - G_p p_\infty(V) (V - E_{Na}) - I_L - I_h \quad (4)$$

$$\frac{dr_f}{dt} = \frac{r_{f,\infty}(V) - r_f}{\tau_{r_f}(V)}, \quad (5)$$

$$\frac{dr_s}{dt} = \frac{r_{s,\infty}(V) - r_s}{\tau_{r_s}(V)}. \quad (6)$$

As in Eq. (1), $I_h = G_h (0.65 r_f + 0.35 r_s) (V - E_h)$ and $I_L = G_L (V - E_L)$. For future use we call $I_{h_f} = G_h 0.65 r_f (V - E_h)$ and $I_{h_s} = G_h 0.35 r_s (V - E_h)$. Our simulations with the full SC model (1)-(3) show (data not presented here)

that $I_{Na} < I_{h_s}$ during the ISI where STOs occur. In fact, one could describe this ISI as the interval of time for which I_{Na} and I_K are inactive in the sense that they are much lower than the ISI I_h , I_{Nap} and I_L currents.

The voltage bounds during the ISI change with different values of I_{app} and G_h . However, the reduction of dimensions argument used before remains valid over a large range of these parameters.

3.2.2 Reset of I_h

The behavior of v , r_f and r_s are illustrated in Fig. 3. (The second panel is a blow-up of the first.) During a spike, v increases above zero to a value ~ 50 mV. For these values of v , $r_{f,\infty}(v) \sim 0$ and $r_{s,\infty}(v) \sim 0$ (see Fig. 1-a). In addition, for these high values of v , both $\tau_{r_f}(v)$ and $\tau_{r_s}(v)$ are very small (see Fig. 1-b and -c), and then both r_f and r_s quickly decrease to values close to $r_f \sim r_s \sim 0$. In our approximation we take $r_f = r_s = 0$ as initial conditions for the h-current gating variables in the ISI regime (after a spike has occurred).

3.2.3 A stellate cell generalized integrate and fire model

The fact that I_{Na} and I_K are inactive during the ISI suggests that if one is not interested in the spike details but only in the generation of a spike, the dynamics of the SC can be approximately described by a generalized integrate-and-fire (GIF) model consisting of eqs. (4)-(6) supplemented with a threshold for spike generation, v_{th} , and a reset value of the membrane voltage, v_{rst} . Appropriate values of v_{th} should reflect the fact that when crossing threshold, trajectories move towards the spiking regime. In our simulations we use

$$v_{th} = -10 \text{ mV} \quad \text{and} \quad v_{rst} = -80 \text{ mV}. \quad (7)$$

As will be clear later, more negative values of v_{th} may be good as well.

In the full SC model there is a brief intermediate regime in between the spiking regime and the STO regime studied here (ISI). This regime corresponds to the recovery of the voltage after a spike. It is different from the ISI regime studied here in that I_K is an active current and its gating variable n evolves on a time scale faster than both r_f and r_s ; i.e.. n is a dynamic variables interacting with v . We disregard this regime in our generalized integrate and fire (GIF) formulation.

Two- and three-dimensional GIF models have already been proposed in the literature (Izhikevich 2001; Richardson et al. 2003). In the GIF models used by Richardson et al. (2003) to study resonance effects, there is either a two-component I_h or a I_{Nap} and I_{Ks} (slow K^+ current). To our knowledge no GIF model has been proposed having both I_h and I_{Nap} . Our GIF model describes the ISI with asymptotic accuracy and is a good approximation of the full SC model (1)-(3).

In the following sections we study the dynamics of the SC using the reduced description studied here.

3.3 Dynamics of the reduced SC model

In this Section we study the mechanism of generation of STOs in the SC model. These STOs are generated from the dynamics of eqs. (4)-(6).

3.3.1 Canard structures and a study of the reduced model with r_s fixed

The classic canard phenomenon is a sudden explosion of the small amplitude limit cycle created in a Hopf bifurcation (HB). This small amplitude limit cycle can be stable or unstable according to whether the HB point is supercritical or subcritical respectively. Here, we are concerned with the structure near an unstable limit cycle, and not the canard explosion itself. In most of this section, we discuss in as much generality as possible the structure that we use in analyzing our model. For easy applicability to (4-6), we use notation tailored to the model. For a more thorough introduction, we refer the reader to Eckhaus (1983); Krupa and Szmolyan (2001); Dumortier and Roussarie (1996).

The general equations have the form

$$\begin{cases} dv/dt = F(v, r_f; r_s), \\ dr_f/dt = \epsilon G(v, r_f), \end{cases} \quad (8)$$

where $0 < \epsilon \ll 1$ and r_s is a fixed parameter. We assume that $F = \mathcal{O}(1)$ and $G = \mathcal{O}(1)$, so that the two equations in (8) have well-separated time scales. We call $r_f = N(v; r_s)$ the nullcline of the v equation (given by $F(v, r_f, r_s) = 0$).

The dependence of F on r_s is assumed to be such that, as r_s increases, $N(v; r_s)$ moves downward, possibly changing its shape. This is illustrated in

4-a where $\alpha > 0$. We call $P(r_s)$ the fixed point of (8) corresponding to the leftmost intersection of the $N(v; r_s)$ with nullcline of r_f . Note that with the shape of $N(v; r_s)$ as in Fig. 4-a, $P(r_s)$ moves to the right as r_s increases.

We call $r_{s,M}$ the value of r_s corresponding to the nullclines intersecting at the maximum of $N(v, r_s)$. In Fig. 4-a, α is very close to $r_{s,M}$. We further assume that eqs. (8) have a subcritical (unstable) Hopf bifurcation point P_H at some value $r_{s,H} = r_{s,M} + \mathcal{O}(\epsilon)$ close to the maximum of $N(v; r_s)$. We also assume that for each r_s there is a point $P_B(r_s)$ on the left branch of $r_f = N(v; r_s)$ ($r_s < r_{s,M}$), having the property that it separates those fixed points that are stable nodes from those that are stable spirals. In our model, without loss of generality, we are starting with $r_s = 0$. For $r_s = 0$, we assume $P_B(0)$ is to the right of $P(0)$ and for $r_s = \alpha$, $P_B(\alpha)$ is to the left of $P(\alpha)$; our analysis uses that. Our assumptions reproduce the conditions of the real model for the parameters of interest. Note that, in the real model, the reset of I_h due to a spike (see Section 3.2.2) brings the trajectory to the initial condition $r_s = 0$.

There is another value, $r_{s,c}$, of r_s at which the canard explosion occurs (in the limit of $\epsilon \rightarrow 0$). This value is smaller than $r_{s,H}$. Figure 4-b schematically shows the bifurcation diagram, including $r_{s,H}$ and $r_{s,c}$, for a subcritical Hopf bifurcation. Note that the separation of scales in system (8) is necessary for the existence of the canard explosion.

Figure 5 illustrates the three behaviors of the system for different values of r_s in the presence of the above assumptions. In all three cases, we consider trajectories that first approach the v-nullcline and then stay close to it, moving slowly (Fig. 5-a). That there are such trajectories is a consequence of the separation of time scales and the existence of an attracting invariant manifold close to the nullcline. The trajectory we are interested in (coming from the end of a spike) has this property. For values of $r_s \geq 0$ such that $P(r_s)$ is to the left of $P_B(r_s)$, such trajectories approach the fixed point without oscillation; the attraction comes from the stability of the critical point $P(0)$. This is shown in (Figure 5-a).

For a value of $r_s > 0$ such that $P(r_s)$ is to the right of $P_B(r_s)$ but is still stable, the critical point has trajectories spiraling inward. In this situation, as in the previous paragraph, the separation of time scales shapes the nature of the trajectories approaching the critical point. The trajectories now traverse across the maximum of $r_f = N(v; r_s)$ (Figure 5-b). There is still an invariant manifold close to the v-nullcline, but its attractiveness changes (in the limit as ϵ goes to zero) to unstable to the right of the maximum. Nevertheless,

the trajectory stays close to that invariant manifold in the “top” part of each spiral. This is what we refer to as the “canard structure”, and it is related to the mechanism by which small amplitude limit cycles blow up into large relaxation ones.

For some value of r_s still larger, the relevant trajectories do not spiral around the maxima of the v-nullcline (Fig. 5-c). Instead, the trajectory moves across the maximum, close to the unstable small amplitude limit cycle created in the subcritical Hopf bifurcation, and leaves its neighborhood. Note that, in two dimensions, the requirement that trajectories do not cross each other prevents them from spiraling in, as long as an unstable small amplitude limit cycle surrounds the stable fixed point $P(r_s)$. For values of $r_s > r_{s,H}$ the fixed point $P(r_s)$ changes from stable to unstable and there is no longer an unstable limit cycle. In principle, trajectories starting close enough to $P(r_s)$ spiral out and finally leave the $N(v; r_s)$ knee neighborhood. However, the trajectories we are interested in have initial conditions far away from $P(r_s)$, and they approach the knee and leave its neighborhood without spiraling out.

In the above discussion, the separation of time scales was assumed, using $\epsilon \ll 1$. In (4-5), this separation of scales during the ISI studied here is intrinsic to the system. It can be uncovered by defining $\epsilon = G_L^{-1} = 0.025$ and rescaling the system $t \rightarrow \epsilon t$. We do not pursue this here. From (4-5) the v-nullcline is now given by

$$N(v; r_s) = \frac{I_{app} - G_p p_\infty(v) (v - E_{Na}) - G_h 0.35 r_s (v - E_h) - G_L (v - E_L)}{G_h 0.65 (v - E_h)}. \quad (9)$$

Equations (4-5) satisfy the hypotheses above: As r_s is increased, $N(v; r_s)$ moves downward (with a change of shape), and the leftmost critical point $P(r_s)$ moves to the right. A standard stability analysis (not given here) shows that, for the lowest values of r_s , $P(r_s)$ is a stable node, as in Fig. 5-a. As r_s is increased, $P(r_s)$ becomes a stable focus (Fig 5-b). For a still larger value, the system undergoes a subcritical Hopf bifurcation in the neighborhood of $N(v; r_s)$. At still larger values of r_s , the trajectory leaves the neighborhood of the nullcline without oscillations. Indeed, Fig. 5a-c were drawn from eqs. (4-5). For the full equations (1-3), leaving the neighborhood of the nullcline, with or without oscillations, corresponds to leaving the regime of the

reduced equations and going into a regime in which the spiking components are important.

The time spent in the oscillations (decaying or expanding) is closely related to the time the trajectory of (4-6) spends in a subthreshold oscillation (STO). Thus, the canard structure, which forces the trajectory to stay close to the invariant manifold at the “top” portion of the oscillations and imposes a time scale for the STO.

3.3.2 A three-dimensional approach: Generation of subthreshold oscillations

Here we study system (4)-(6). $\tau_{r_f} < \tau_{r_s}$ and $r_{s,\infty}(v) \sim r_{f,\infty}(v)$ (see Fig. 1), so eq. (6) is slower than (5). The rescaling mentioned in Section 3.3.1 (not presented here) confirms that. This is illustrated in Fig. 3 (the second panel is a blow up of the first one). It is evident, by comparing the last two panels, that r_s evolves slower than r_f at the beginning of the ISI. In the middle of the ISI v and r_f engage in a STO. r_s evolves slowly and continues to increase. The assumption $dr_s/dt \ll dr_f/dt$ is not satisfied, so the problem can not be put in the slow passage problem framework used by other authors; e.g. Baer et al. (1989). However, the separation of scales is still large enough to allow the study of the dynamics of eqs. (4)-(6) by looking at slowly evolving phase planes for eqs. (4)-(5), each one corresponding to a constant value of r_s . Three dimensional problems with one fast and two slow variables have been treated using different approaches by other authors (Wechselberger 2004; Drover et al. 2004). Here we focus on a heuristic explanation of the mechanism of generation of STOs and the transition from STOs to spikes in the reduced SC model.

The dynamics of the reduced system can be heuristically explained by looking at phase planes of the type discussed in Section 3.3.1 continuously evolving with r_s . We illustrate this in Fig. 6. The schematic Fig. 4-a is helpful in this explanation too. As r_s evolves, the v -nullcline $N(v; r_s)$ continuously moves down, generating a two-dimensional slow manifold. $P(r_s)$, which is also continuously evolving, generates a curve (in Fig. 4-b this curve contains the points $P(0)$ and $P(\alpha)$ and it is contained in the r_f -nullcline). There are two other relevant curves parametrized by r_s , the fold curve L joining the maxima of $N(v; r_s)$ and the separatrix curve L_B joining the points $P_B(r_s)$ (not shown in the Figs.). As r_s increases, $r_{f,\infty}$ intersects both L and L_B . Note that by intersecting the nullsurface $N(v; r_s)$ with planes $r_s = k$

($k > 0$ constant) one recovers the nullclines $N(v; k)$ corresponding to two-dimensional systems, as described in Section 3.3.1. Values of $P(r_s)$ to the left of L_B and close enough to L_B correspond to stable foci in $N(v; k)$, and for some value of r_s such that $P(r_s)$ is to the right of L , $P(r_s)$ is to the left of the HB point. We use both two- and three-dimensional approaches in our explanation.

Due to the separation of time scales, the trajectory \mathcal{T} starting at $(v_0, r_{f,0}) = (-80, 0)$ stays close to the manifold $N(v; r_s)$ (Fenichel 1971) and moves towards $P(r_s)$. The 2D points $P(r_s)$ are not fixed points (in the three-dimensional view), so there is no convergence to them; they are target points towards which the trajectory moves. Note that the speed of r_s in Fig. 3 is not constant, but decreases as r_s increases. When \mathcal{T} gets close enough to the knee of $N(v; r_s)$ and r_s is such that $P(r_s)$ corresponds to a focus in a two-dimensional view, \mathcal{T} oscillates around the knee, staying close to the slow manifold $N(v; r_s)$. In this two-dimensional view, this corresponds to “spiraling down” to a fixed point. Note that \mathcal{T} can get inside the “limit cycle” because of the extra dimension in the 3D system. As r_s increases further, $P(r_s)$ is to the right of the HB point and the trajectory escapes this regime to the spiking one, where I_{Na} and I_K get activated. Note that the spike is produced at almost the same voltage at which the previous STO reached its maximum. That means that the phase of the STOs at which a spike is produced is governed by the canard structure.

The amplitude of the oscillations decreases as $P(r_s)$ approaches the curve L (joining the maxima of $N(v; r_s)$) and increases again for values of $P(r_s)$ to the right of L . This is illustrated in Fig. 6 (see also Fig. 5 for a comparison with the two-dimensional case). Past the HB point, the unstable limit cycle has disappeared, so there is no impediment to spiraling outwards in the locally relevant 2D analogue.

The number and amplitude of the STOs is affected by the speed of r_s : The slower r_s , the more STOs are developed, since \mathcal{T} spends more time near the knee. On the other hand, if r_s evolves fast enough, \mathcal{T} does not spend enough time near the knee for even one STO to be generated. In the reduced SC model, the speed of r_s is not uniform but decreases with time (see Fig. 3). To the first approximation, it is faster for values of $r_s < r_{s,M}$ ($P(r_s)$ to the left of the curve L) than for values of $r_s > r_{s,M}$. Thus, there may be fewer STOs with decreasing amplitude. As a consequence the STOs with decreasing amplitude are hard to see.

3.4 Robust subthreshold oscillations in a noisy GIF SC model

In Section 3.3 we explained the mechanism of generation of STOs for the reduced SC model, which is deterministic. One of the features of deterministic SC models is that, for physiologically plausible parameters (and consequent speeds of r_s), STOs and mixed mode patterns are unlike those seen in experiments. If the STOs generated by the SC model do not decay to resting potential, they increase their amplitude. Simulations show that an action potential is fired, as shown in Figs. 6-c and 7-a. In this case, the pattern repeats itself at a roughly constant period. In experiments, however, when the membrane potential is depolarized from resting potential to a value below spiking threshold, STOs at a theta frequency are generated with no apparent amplitude pattern. As the membrane potential approaches spiking threshold, SCs fire action potentials with no clear regular firing pattern. See Section 1 for references.

Various modeling studies have introduced channel noise in order to obtain robust STOs. White et al. (1998) showed that the number of persistent Na^+ channels underlying STOs is relatively small and argued that the stochastic behavior of these channels may contribute crucially to the cellular-level responses. In their study they used a biophysical stochastic-deterministic model having I_{Nap} and I_{Ks} in addition to the standard HH currents. The I_{Nap} they used was represented by a population of stochastic ion channels. Using this model they found regimes in which STOs and spikes coexist. More recently, Fransén et al. (2004) used a noisy model having I_{Nap} and a two-component I_h . They concluded that, although noise is not required for the SC to display STOs, its presence increases their robustness.

Here we want to explain how the effects of noise can be understood using the canard structure framework explained in previous sections. For this we introduce channel white noise in I_{Nap} . We do that in a very simple way, not claiming it to be biophysically plausible, but simple enough to give a heuristic explanation of the mechanism of generation of robust STOs due to noise effects. We add a stochastic term $\sqrt{2D}\eta(t)$ to the dynamic equation for p . This term is delta correlated with zero mean; i.e., $\langle \eta(t), \eta(t') \rangle = \delta(t - t')$. $D > 0$ is the standard deviation. Since p is slaved to v , we substitute $p_\infty(v) + \tau_p(v) \sqrt{2D} \eta(t)$ for $p_\infty(v)$ in in eq. (4).

In order to get results qualitatively similar to the findings of other authors (see Fransén et al. (2004), for an example) we set the value of the tonic drive

to $I_{app}^0 = -2.58$, so that in the absence of noise the SC is silent but the system is very close to $P_B(0)$ (see Fig. 4-a). In Fig. 7-a we show the voltage trace for a noiseless system ($D = 0$) driven at $I_{app} = -2.55 > I_{app}^0$ up to the time where the first spike occurs. In Fig. 7-b we show the voltage trace for $D = D_M = 10^{-6}$ and I_{app}^0 . D_M is approximately the largest value of D for which the SC displays only STOs in the time interval considered. For larger values of D the SC fires at least one spike in this interval.

In Fig. 7-c we compare the voltage trace of the SC presented in Fig. 7-b with a 10 Hz sinusoidal function to show that the noisy SC oscillates at approximately this frequency. The power spectrum of the STOs in Fig. 7-b and -c have a well defined peak at 10 Hz (data not shown).

If one chooses a lower value of I_{app} (making the intersection point between nullclines further to the left of $P_B(0)$), one can still get STOs with a theta frequency component provided the value of D is increased. Because of the increase in D , the voltage traces look noisier than in the former case. As an illustration, Fig. 7-d shows the voltage traces for $I_{app} = -2.7$ and $D = 2.5 \times 10^{-5}$. There the agreement with a 10 Hz sinusoidal function is not as good as in the previous case discussed. The power spectrum for this case still has a peak centered at 10 Hz but it is wider.

In all cases, as D decreases the frequency preference is kept, but the amplitude of the STOs decreases. Qualitatively similar results have been obtained for other similar parameters regimes. In all cases considered, robust STOs similar to the ones shown in Fig. 7-b were found, provided I_{app} was slightly lower than the boundary value $P_B(0)$ above which the fixed point is a stable focus.

For the case described above, a heuristic explanation of the effect of noise can be achieved by using the canard structure framework described in former sections. As before we view the dynamics of the three dimensional system as a two-dimensional system with r_s moving the v -nullcline $N(v; r_s)$ downwards. In the absence of noise, the intersection of $N(v; r_s)$ and $r_{f,\infty}(v)$ determine four regions inside which the trajectory \mathcal{T} evolves, as schematically shown in Fig. 8, targeting the 2-D fixed point in a monotonic or oscillatory way. The effect of noise is to randomly move $N(v; r_s)$ and consequently, to randomly move the “fixed point” (intersection between nullclines). As this happens, the tip of the trajectory, $\mathcal{P}(t)$ may find itself in any of the four regions. For as long as this situation persists, \mathcal{T} evolves, targeting the fixed point as schematically shown in Fig. 8.

A distinguished situation occurs when \mathcal{T} is in R_{II} . In this case, \mathcal{T} is

forced to move around the knee of $N(v; r_s)$ before crossing $N(v; r_s)$ to R_{III} . In this way an oscillation is obtained with a similar frequency to its noiseless counterpart. It may occur that, before finishing the oscillation, $\eta(t)$ is large enough to move $N(v; r_s)$ up, leaving \mathcal{T} in R_{II} , and this effect lasts for enough time so to prevent the oscillation. However, for small enough values of D , the probability that this happens is very low. So once \mathcal{T} is in R_{II} it will produce a STO with high probability and at the frequency established by the canard structure. For values of D larger than some D_M , the noisy SC will produce a spike in a given time interval for which there are no spikes when $D = D_M$. For very small values of D ($D < D_M$), one gets STOs with the same frequency content as for $D = D_M$ but with smaller amplitude.

If the parameters of the model are such that $N(v; r_s)$ and $r_{f,\infty}(v)$ intersect at a stable node below and not very close to P_B , then one needs a larger value of D (than in the case described in the former paragraph) for \mathcal{T} to get to the knee of $N(v; r_s)$ where, due to the canard structure, one get STOs. In this case the STOs will look very noisy.

3.5 Synchronization properties of networks of GIF SC models

It has been argued that I_h plays a relevant role in determining the synchronization properties of networks including SCs and other cells having similar electric properties (Acker et al. 2003; Netoff et al. 2004; Rotstein et al. 2004; Jalicis et al. 2004). Among the latter we mention the oriens lacunosum-moleculare (O-LM) cells in the hippocampus (Gillies et al. 2002). Since the effects of I_h are captured by the GIF SC model, we use equations (4,6,7) instead of the full SC model in our network synchronization studies and compare our results with previous findings.

To consider the effect of synaptic currents to each SC we add a synaptic term $-I_S$ to the current-balance equation (4)

$$C \frac{dV}{dt} = I_{app} - G_p p_\infty(V) (V - E_{Na}) - I_L - I_h - I_S \quad (10)$$

where $I_S = G_S S (v - E_{rev})$ and $E_{rev} = E_{ex} = 0 \text{ mV}$ or $E_{rev} = E_{in} = -80 \text{ mV}$, for excitatory or inhibitory synaptic connections respectively. The synaptic variable S we used is given by (Dayan and Abbott 2001)

$$S = S_N (e^{-t/\tau_1} - e^{-t/\tau_2}), \quad \text{with} \quad S_N = \left[\left(\frac{\tau_2}{\tau_1} \right)^{\tau_{rise}/\tau_1} - \left(\frac{\tau_2}{\tau_1} \right)^{\tau_{rise}/\tau_2} \right]^{-1}. \quad (11)$$

We define the decay time τ_{dec} as the time it takes S to decay from its maximum value to 0.37 % ($1/e$) of its maximum value. Below, the units of τ_1 , τ_2 and τ_{dec} are msec, and the units of G_S are mS/cm^2 . We performed simulations for different natural frequencies of the SCs in the theta range (8 - 12 Hz). The natural frequency of a cell is its firing frequency when uncoupled.

We consider different types of networks in which excitatory and/or inhibitory connections are present. SCs are excitatory and they are connected via AMPA. The SC full model has been used for O-LM cells in the hippocampus (Rotstein et al. 2004). In contrast to the SCs, O-LM cells are inhibitory mediated by GABA_A as are other inhibitory neurons (IN) present in excitatory/inhibitory networks including SCs. We used various kinetics for both AMPA and GABA_A summarized in Table 1. The AMPA¹ and AMPA² kinetics have been considered by Acker et al. (2003) and Netoff et al. (2004) respectively. The GABA_A¹ kinetics has been considered by Netoff et al. (2004). The GABA_A² kinetics is standard (Destexhe et al. 1994; Dayan and Abbott 2001) and then worth considering, but has not been used in networks including SCs. The GABA_A³ and GABA_A⁴ kinetics correspond to values used by Rotstein et al. (2004) for O-LM cells.

Our simulations show that two SCs connected via AMPA¹ and AMPA² synchronize at theta frequencies for values of G_S up to ~ 0.089 and ~ 0.065 respectively and natural frequencies of 12 Hz. For higher values of G_S the networks fire in antiphase at a much higher frequency (~ 50 to 60) Hz. The results are qualitatively similar for SC natural frequencies in the 8 - 12 Hz range. All this is consistent with the findings by Acker et al. (2003) and the results obtained using the full SC model.

Simulations of SCs connected via inhibition using the four values for the GABA_A kinetics (see Table 1) show that for physiological values of G_S , the networks displayed an antiphase firing pattern as predicted experimentally and theoretically (Netoff et al. 2003; Rotstein et al. 2004).

To study the effect of common inhibition on two uncoupled SCs we connect an interneuron (IN), using a standard Hodgkin-Huxley model, to the two SCs using GABA_A¹ synaptic connections (see Table 1) as in (Netoff et al.

Synapse type	τ_{dec}	τ_1	τ_2
AMPA ¹	6.15	5.30	0.78
AMPA ²	8.13	6.21	1.68
GABA _A ¹	6.96	5.00	1.68
GABA _A ²	5.92	5.60	0.28
GABA _A ³	10.00	9.70	0.30
GABA _A ⁴	20.00	19.70	0.30

Table 1:

2004). The IN is set to fire rhythmically over a large range of frequencies (from 8 up to ~ 60 Hz). The natural frequency of the SC is 10 Hz and $G_s = 0.1$. We show our results in Fig. 9. The results are qualitatively similar for other SC natural frequencies in the theta range (8 - 12 Hz).

For IN firing frequencies in the theta range, the SCs synchronize and the IN impose their frequency on the SCs (see Fig. 9-a). For IN firing frequencies slightly above the theta range, the IN input is fast enough to suppress some of the SC spikes (see Figs. 9-b). In this case, the timing of the SC firing is such that an input from the IN may advance the spiking of one of the SCs and delay the other. In general, the patterns obtained are not coherent, though they may be for some choice of parameters with the two SCs firing in antiphase (data not shown). For higher frequencies, more coherent patterns (in-phase, antiphase, with a phase lag of one third of a period) can be obtained (see Fig. 9-c and -f). For these frequencies, the IN fires fast enough to suppress some of the SC spikes. The natural driving currents of the SC cannot withstand the inhibition. However, I_h (activated by inhibition) comes into play. Each time there is a pulse of inhibition, this current builds up until the SC fires and I_h resets. During this process, the SC displays STOs with increasing amplitude. Depending on initial conditions,

SC may phase-lock to different cycles of the IN, resulting in the patterns shown in Figs. 9-c to -f. Note that in Figs. 9-c and -d the SC frequency is half the IN frequency (1 STO per spike) while in Figs. 9-e and -f, the SC frequency is a third of the IN frequency (2 STOs per spike). In the latter case, the IN frequency is too high for the SC to overcome inhibition in only one cycle; i.e., after the SC fires the IN hits the SC twice before the I_h builds up and allows the SC to fire again.

As the IN frequency increases, the number of STOs per spike also increases (Figs.9-c to g); it takes an increasing number of cycles for the h-current to build up enough to overcome the inhibition (Kopell and LeMasson 1994). For IN firing at ~ 42 Hz, the SC firing is completely suppressed; i.e. the h-current is not able to increase to high enough values as to allow the SC voltage to reach threshold (Fig.9-h). This qualitatively matches simulations done with similar equations (Rotstein et al. 2004).

4 Discussion

Subthreshold membrane potential oscillations have been observed at various locations in the brain (Alonso and Llinás 1989; Dickson et al. 2000b; Hutcheon et al. 1996; Llinás and Yarom 1981, 1986; Erchova et al. 2004). In the last years, the study of STOs in the MEC has received special attention from both the experimental and theoretical point of view (see references in Section 1). The results presented in this manuscript contribute to the understanding of the biophysical mechanism of this phenomenon.

It was already known that the interaction between I_{Nap} and I_h is enough to account for the generation of STOs in layer II of the MEC. However, the specific role of each one of these currents, in particular, the fast and slow components of I_h , and the dynamics of their interaction, was not yet understood. To answer these questions we looked at a biophysical single-cell model that has been used in the past to study synchronization properties of SCs. We demonstrated that this seven-dimensional model can be approximated by a reduced three-dimensional model in the ISI, where STOs are observed. This approximation is based on the fact that the spiking generation currents (I_{Na} and I_K) are not active in the ISI regime. Furthermore, there is a clear separation of scales between the three dynamic variables. This, together with the arrangement of the nullsurfaces in the three-dimensional phase space creates what we call the canard structure. This structure serves as the basic

framework to understand the dynamic aspects of the generation of STOs and the coexistence of STOs and spikes. In the absence of r_s as a dynamic variable, the v and r_f nullclines intersect at a fixed point that is a stable node, stable focus or unstable focus. Thus, trajectories can either converge to a fixed point (in an oscillatory fashion or not) or spike. No mixed-modes are possible. The role of r_s , evolving on the slowest time scale of the system, is, roughly speaking, to serve as a bridge between both dynamic behaviors, allowing for coexistence of STOs and spikes. Each time a trajectory moves around the knee it has to “decide” whether to cross the v nullcline or escape the subthreshold regime, producing a STO or a spike respectively. The value of v at which this happens is the one corresponding the peak of a STO. So, the canard structure approach explains why spikes occurs at the peak of the STOs, as experimentally found (Dickson et al. 2000b).

The structural dynamic ideas presented here are consistent with previous theoretical observations by (Fransén et al. 2004) who concluded that the fast component is the major factor in the oscillation generation. Simulation of the partial blockade (65%) of I_h by cesium caused a decrease in the amplitude and frequency of STOs corresponding to that observed in current-clamp recordings. Full block of I_h completely abolished the oscillations. These findings can be explained in terms of the canard structure discussed here. Our calculations show that blockade (partial or total) of I_h has the effect of changing the voltage nullcline $N(v; r_s)$ in such a way that either the knee disappears or the stable fixed point $P(0)$ is farther away from the knee, requiring a quicker time scale for r_s or a larger value of G_h to be able to reach the STO regime (associated with this knee). We develop these ideas further in a future paper.

The patterns of activity seen in experiments are very irregular, in contrast to the regular patterns (a constant number of STOs per spike) obtained in our deterministic SC model. In terms of the canard mechanism proposed in this paper, the occurrence of a spike can be thought of as a loss of stability of the STO regime (a spiking instability). In related theoretical work, stochastic models, with persistent sodium channel noise, have been successfully used to enhance the robustness of STOs (White et al. 1998). In Section 3.4 we obtained the same result in our GIF SC model and we identified conditions under which the STOs are very close to a sinusoidal function. One potential explanation for the effect of noise in enhancing the robustness of STOs might be that noise suppresses spikes; i.e., noise prevents spiking by moving the voltage nullcline in a way that forces the trajectory to stay away from the spiking instability. However, our theoretical approach (using the canard

structure) suggests that this is not the case. The most robust STOs are obtained when, in the absence of noise, the SC is silent but close to STO activity. The effect of noise is to force the system to move around the knee of the voltage nullcline, thus creating a STO. In this sense, noise creates an “intermediate STO state” in between silence and STO/spiking. Once the trajectory moves around the knee the effect of noise is minimal. If the noise amplitude (D) is too big, a spike can be produced. Otherwise, the trajectory returns to the fixed point where noise becomes important again and can drive the trajectory to a new STO excursion.

The function of STOs is not clear yet, but they are believed by some to play a role in synchronization and other coherent dynamic behavior (Hutcheon and Yarom 2000; Dickson et al. 2000a; Buzsáki and Draguhn 2004). We studied the synchronization properties of networks including SCs using the GIF presented in Section 3.2.3. Our results are qualitatively similar to other studies that used the full SC model (Acker et al. 2003; Netoff et al. 2004; Rotstein et al. 2004; Pervouchine et al. 2004). We hypothesize that the canard structure, created by the same equations used in the GIF SC model, is responsible for the dynamics producing the coherent behaviour, rather than the existence of STOs per se.

Problems with similar mathematical structure as the one given by eqs. (4)-(6) have been studied by Wechselberger (2004) and Drover et al. (2004) in order to explain the spike-frequency reduction of a Hodgkin-Huxley neuron due to excitatory synaptic self-coupling. In both cases, a two-dimensional system with fast (V) and slow (h) variables was used to model the dynamics of the neuron, and an extra slow variable was used for an autapse on the neuron. The two approaches are different but complementary. The reduction of spiking frequency is the result of the trajectory being trapped in a neighborhood of a fold line (L in our notation). As in our model, STOs (or MMOs) are observed in a neighborhood of L . However, in the SC model, the STOs are intrinsically generated by the single cell with no need of a synaptic self-coupling.

In this work we give heuristic arguments to explain the generation of STOs in the SC model. Work in progress, including the development of reduction of dimension techniques (Rotstein et al. 2005) and the application of the theory developed by Wechselberger (2004), aims to make the justifications of the reductions to the GIF model and the generation of STOs more precise.

Acknowledgments

The authors want to Andreas Herz, Steve Epstein and Carson Chow for fruitful discussions.

This work was partially supported by the Burroughs Wellcome Fund (HGR), NIH grant 5 RO1 NS46058 (NK), NSF grant DMS-0211505 (NK) and the graduate program “Dynamics and Evolution of Cellular and Macromolecular Processes” of the German Research Foundation, DFG (TO).

References

- Acker CD, Kopell N, and White JA**, Synchronization of strongly coupled excitatory neurons: relating network behavior to biophysics. *Journal of Computational Neuroscience* 15: 71–90, 2003.
- Alonso AA and Klink R**, Differential electroresponsiveness of stellate and pyramidal-like cells of medial entorhinal cortex layer II. *J Neurophysiol* 70: 144–157, 1993.
- Alonso AA and Llinás RR**, Subthreshold Na^+ -dependent theta like rhythmicity in stellate cells of entorhinal cortex layer II. *NATURE* 342: 175–177, 1989.
- Baer SM, Erneux T, and Rinzel J**, The slow passage through a Hopf bifurcation: delay, memory effects, and resonance. *SIAM J Appl Math* 49: 55–71, 1989.
- Burden RL and Faires JD**, *Numerical analysis*. PWS Publishing Company - Boston, 1980.
- Buzsáki G and Draguhn**, Neuronal oscillations in cortical networks. *Science* 304: 1926–1929, 2004.
- Chow CC and White JA**, Spontaneous action potentials due to channel fluctuation. *Biophysical J* 71: 3013–3021, 1996.
- Dayan P and Abbott LF**, *Theoretical Neuroscience*. The MIT Press, 2001.

- Destexhe A, Mainen ZF, and Sejnowski TJ**, Synthesis of models for excitable membranes, synaptic transmission and neuromodulation using a common kinetic formalism 3: 195–230, 1994.
- Dickson CT, Magistretti J, Shalinsky M, Hamam B, and Alonso AA**, Oscillatory activity in entorhinal neurons and circuits. *Ann NY Acad Sci* 911: 127–150, 2000a.
- Dickson CT, Magistretti J, Shalinsky MH, Fransén E, Hasselmo M, and Alonso AA**, Properties and role of I_h in the pacing of subthreshold oscillation in entorhinal cortex layer II neurons. *J Neurophysiol* 83: 2562–2579, 2000b.
- Drover J, Rubin J, Su J, and Ermentrout B**, Analysis of a canard mechanism by which excitatory synaptic coupling can synchronize neurons at low firing frequencies. *SIAM J Appl Math*, to appear 2004.
- Dumortier F and Roussarie R**, Canard cycles and center manifolds. *Mem-oirs of the American Mathematical Society* 121 (577), 1996.
- Eckhaus W**, Relaxation oscillations including a standard chase on french ducks. *In Lecture Notes in Mathematics, Springer-Verlag* 985: 449–497, 1983.
- Erchova I, Kreck G, Heinemann U, and Herz AVM**, Dynamics of rat entorhinal cortex layer II and III cells: characteristics of membrane potential resonance at rest predict oscillation properties near threshold. *J Physiol* 560: 89–110, 2004.
- Fenichel N**, Persistence and smoothness of invariant manifolds for flows. *Ind Univ Math J* 21: 193–225, 1971.
- Fransén E, Alonso AA, Dickson CT, and Magistretti ME J Hasselmo**, Ionic mechanisms in the generation of subthreshold oscillations and action potential clustering in entorhinal layer ii stellate neurons. *Hippocampus* 14: 368–384, 2004.
- Fransén E, Dickson CT, Magistretti J, Alonso AA, and Hasselmo ME**, Modeling the generation of subthreshold membrane potential oscillations of entorhinal cortex layer II stellate cells. *Soc Neurosci Abstr* 24: 814.815, 1998.

- Fransén E, Wallestein GV, Alonso AA, Dickson CT, and Hasselmo ME**, A biophysical simulation of intrinsic and network properties of entorhinal cortex. *Neurocomputing* 26-27: 375–380, 1999.
- Gillies MJ, Traub RD, LeBeau FEN, Davies CH, Gloveli T, Buhl EH, and Whittington MA**, A model of atropine-resistant theta oscillations in rat hippocampal area CA1. *J Physiol* 543.3: 779–793, 2002.
- Hutcheon B, Miura RM, and Puil E**, Subthreshold membrane resonance in neocortical neurons. *J Neurophysiol* 76: 683–697, 1996.
- Hutcheon B and Yarom Y**, Resonance oscillations and the intrinsic frequency preferences in neurons. *Trends Neurosci* 23: 216–222, 2000.
- Izhikevich EM**, Resonate-and-fire neurons. *Neural Networks* 14: 883–894, 2001.
- Jalics J, Kispersky T, Dickson C, and Kopell N**, Neuronal ensembles and modules: modeling dynamics in medial entorhinal cortex. *Society for Neuroscience Abstracts* 517.1, 2004.
- Klink RM and Alonso A**, Ionic mechanisms for the subthreshold oscillations and differential electroresponsiveness of medial entorhinal cortex layer II neurons. *J Neurophysiol* 70: 128–143, 1993.
- Klink RM and Alonso AA**, Ionic mechanisms of muscarinic depolarization in entorhinal cortex layer ii neurons. *J Neurophysiol* 77: 1829–1843, 1997.
- Kopell N and LeMasson G**, Rhythmogenesis, amplitude modulation, and multiplexing in a cortical architecture. *Proc Natl Acad Sci USA* 91: 10586–10590, 1994.
- Krupa M and Szmolyan P**, Relaxation oscillation and canard explosion. *J Diff Eq* 174: 312–368, 2001.
- Llinás RR and Yarom Y**, Electrophysiology of mammalian inferior olivary neurons *in vitro*. different types of voltage-dependent ionic conductances. *J Physiol* 315: 549–567, 1981.
- Llinás RR and Yarom Y**, Oscillatory properties of guinea pig olivary neurons and their pharmacological modulation: an *in vitro* study. *J Physiol* 376: 163–182, 1986.

- Magistretti J and Alonso AA**, Biophysical properties and slow voltage-dependent inactivation of a sustained sodium current in entorhinal cortex layer-II principal neurons. a whole-cell and single-channel study. *J Gen Physiol* 114(4): 491–509, 1999.
- Magistretti J and Ragsdale DS**, High conductance sustained single-channel activity responsible for the low-threshold persistent Na^+ current in entorhinal cortex neurons. *J Neurosci* 19(17): 7334–7341, 1999.
- Makarov VA, Nekorkin VI, and Velarde MG**, Spiking behavior in a noise-driven system combining oscillatory and excitatory properties. *Phys Rev Lett* 15: 3031–3034, 2001.
- Netoff T, Banks M, and White J**, Bridging single cell and network dynamics. *Society for Neuroscience Abstracts* 32 171.7, 2003.
- Netoff T, Pervouchine D, Kopell N, and White J**, Oscillation frequency switches in model and hybrid networks of the hippocampus. *Society for Neuroscience Abstracts* *32*, In press 2004.
- Pervouchine D, others, and Kopell N**. *In preparation* 2004.
- Richardson MJE, Brunel N, and Hakim V**, From subthreshold to firing-rate resonance. *J Neurophysiol* 89: 2538–2554, 2003.
- Rotstein HG, Clewley R, Wechselberger M, and Kopell N**, Dynamics of an entorhinal cortex stellate cell model. *In preparation* 2005.
- Rotstein HG, Pervouchine D, Gillies MJ, Acker CD, White JA, Buhl EH, Whittington MA, and Kopell N**, Slow and fast inhibition and h-current interact to create a theta rhythm in a model of cal interneuron networks. *Submitted* 2004.
- Wechselberger M**, Existence and bifurcation of canards in R^3 in the case of a folded node. *SIAM J Appl Dyn Syst*, to appear 2004.
- White JA, Budde T, and Kay ARA**, A bifurcation analysis of neuronal subthreshold oscillations. *Biophysical J* 69: 1203–1217, 1995.
- White JA, Klink R, Alonso A, and Kay ARA**, Noise from voltage-gated ion channels may influence neuronal dynamics in the entorhinal cortex. *J Neurophysiol* 80: 262–269, 1998.

White JA, Rubinstein JT, and Kay AA, Channel noise in neurons.
Trends Neurosci 23(3): 131–137, 2000.

Table Legends

Table 1: Parameters and decay times (τ_{dec}) for synaptic connections of various kinetic types (AMPA and GABA_A). The units of τ_1 , τ_2 and τ_{dec} are msec.

Figure Legends

Figure 1: Ion channel dynamics for the full SC model (1-3). The gating variables are $x = m, n, h, p, r_f, r_s$. The bottom pannels are magnifications of the top ones in the voltage interval (using mV units) $(-65 : -40)$. (a) Activation and inactivation curves ($x_\infty(V)$) for the gating variables. (b) Voltage-dependent times scales ($\tau_x(V)$) for the gating variables. The separation of time-scales is clearly visible. Both, $\tau_{r,f}$ and $\tau_{r,s}$ evolve on time scales much slower than the other variables. (c) Voltage dependent time scales in a larger time interval.

Figure 2: Changing I_{app} changes the ratio of spikes to STOs in the full SC model. Voltage (V) traces, I_h and I_{Nap} for various values of the applied current I_{app} and $G_h = 1.5$. The values of the other parameters used in the simulations are given in the Appendix. The second row in each panel is a magnification of the first row.

Figure 3: Gating variables during STOs and spikes in the full SC model. Voltage (V), r_f and r_s traces for $I_{app} = -2.5$ and $G_h = 1.5$. The values of the other parameters used in the simulations are given in the Appendix. The second row is a magnification of the first row.

Figure 4: (a) Schematic representation of the nullclines $N(v; r_s)$ and $r_{f,\infty}(v)$ of system (8) for $r_s = 0$ and $r_s = \alpha > 0$. $P(r_s)$ represent fixed points, $P_B(r_s)$ represent points dividing between stable nodes and foci. As α increases the nullcline $N(v; r_s)$ moves down while the activation curve (nullcline) $r_{f,\infty}(v)$ remains unchanged. (b) Schematic bifurcation diagram for a subcritical Hopf

bifurcation. An unstable limit cycle is born at the Hopf bifurcation point $r_{s,H}$ out of a fixed point. This fixed point is stable to the left of $r_{s,H}$, and unstable (to the right of $r_{s,H}$). At the canard critical point $r_{s,c}$ the amplitude of the limit cycle explodes.

Figure 5: Phase plane for the reduced SC model for various values of r_s for $G_h = 1.5$ and $I_{app} = -2.5$. The values of the other parameters used in the simulations are given in the Appendix. Lower panels are magnifications of the upper ones. (a) $r_s = 0$: the trajectory converges to a fixed point without spiraling. (b) $r_s = 0.085$: the trajectory spirals down to a fixed point. (c) $r_s = 0.086$: the trajectory moves around the knee of the nullcline $N(v; r_s)$ and escapes the regime without spiraling.

Figure 6: Dynamics of the reduced SC model for $G_h = 1.5$ and $I_{app} = -2.5$. The values of the other parameter used in the simulations are given in the Appendix. (a) Trajectory for r_f and v when r_s evolves continuously. (b) Magnification of panel (a). Note that when the trajectory escapes the regime (corresponding to the SC firing an action potential), it does so at the same voltage at which the previous STO reached its maximum. (c) voltage trace.

Figure 7: Results of simulations for noiseless and noisy systems for $G_h = 1.5$. The values of the parameter used in the simulations are given in the Appendix. (a) $D = 0$ and $I_{app} = -2.55$. In the absence of noise the amplitude of the STOs increase uniformly with time and eventually the SC fires an action potential. In the figure we show the STOs up until the first spike. For $I_{app} = -2.58$ and $D = 0$ the SC is silent (data not shown). (b) $D = 10^{-6}$ and $I_{app} = -2.58$. STOs are produced in the presence of noise, but the amplitude does not increase uniformly with time. For comparison we show the STOs for the same amount of time as in Fig. (a). (c) $D = 10^{-6}$ and $I_{app} = -2.58$. Comparison of the STOs produced in the noiseless case with a sinusoidal function (10 Hz). (d) $D = 2.5^{-5}$ and $I_{app} = -2.7$. Comparison of the STOs produced in the noiseless case with a sinusoidal function (10 Hz). The value of D is larger as compared to the one in (c) and the STOs are more influenced by noise.

Figure 8: Schematic diagram of the nullclines $N(v; r_s)$ and $r_{f,\infty}(v)$. The arrows show the direction of motion of trajectories. In particular, perturbations to the fixed point evolve in following the arrows.

Figure 9: Results of simulations for two uncoupled SCs receiving GABAergic input from an interneuron at various frequencies. The synaptic function is given by (11) with $\tau_1 = 5$, $\tau_2 = 1.68$ ($\tau_{dec} = 6.96$) and $G_s = 0.1$. The natural frequency of the SCs is 10 Hz, while the natural frequency of the IN is varied and displayed above each plot. As this natural frequency increases different temporal patterns are obtained.

Figures

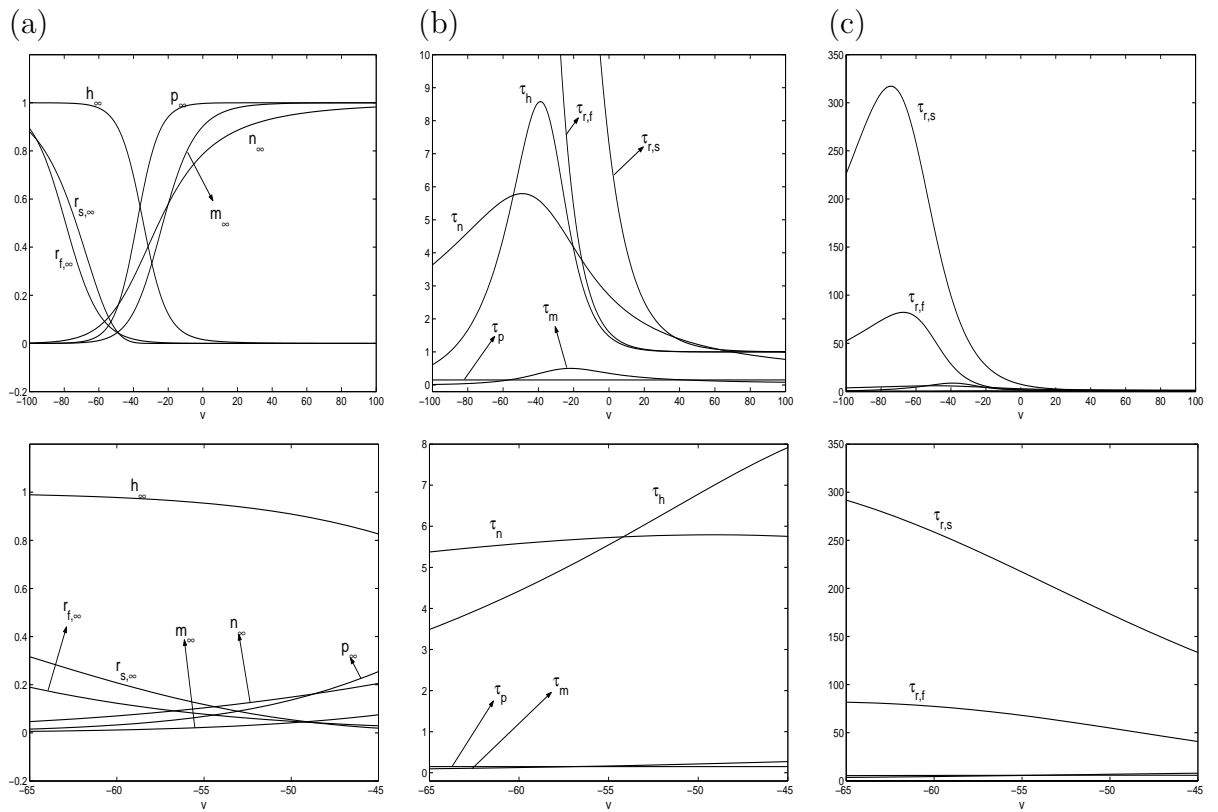


Figure 1:

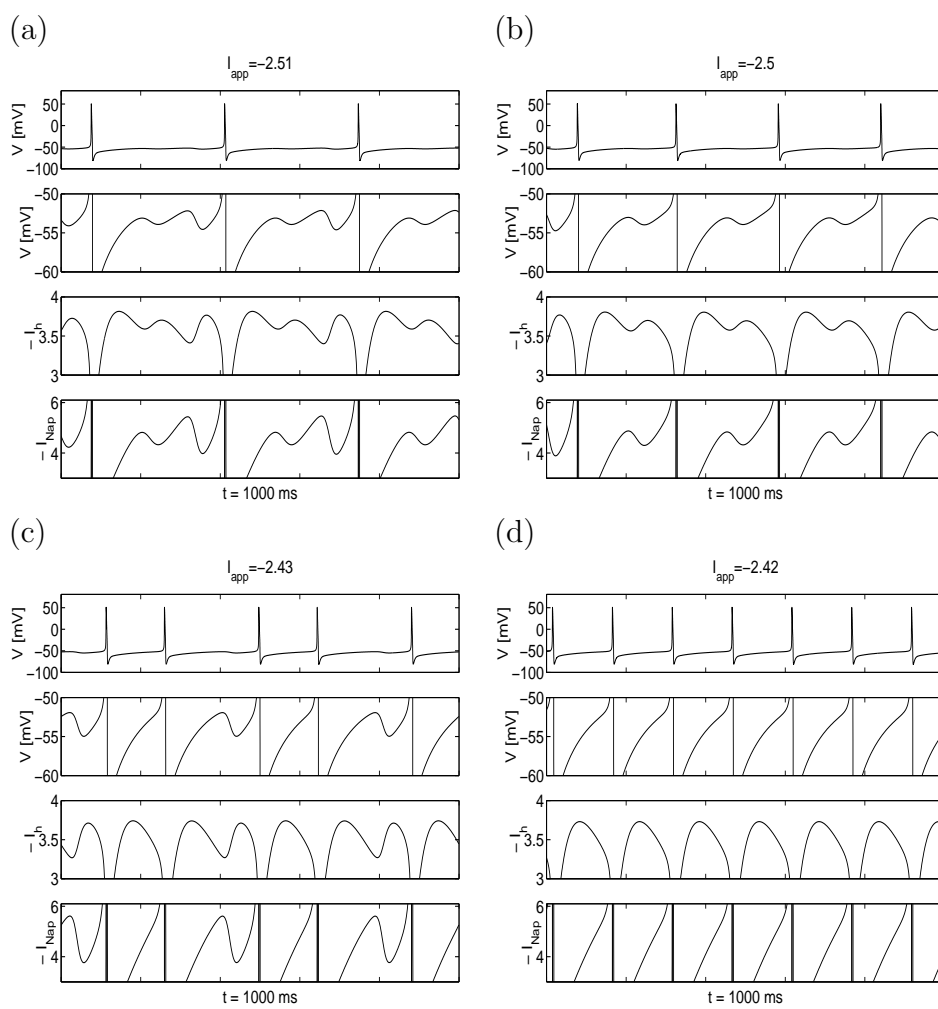


Figure 2:

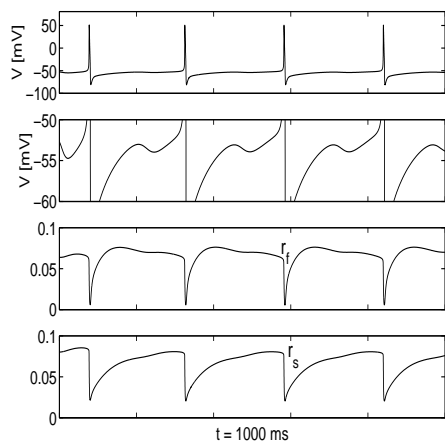


Figure 3:

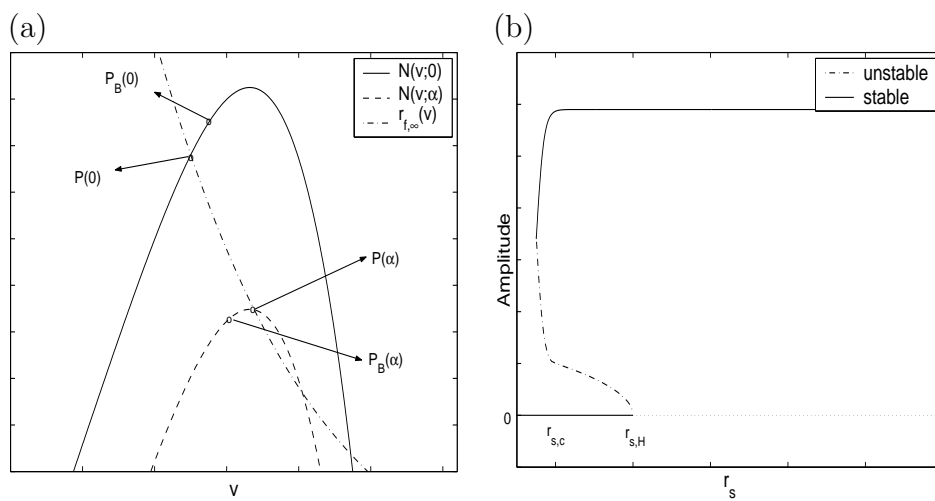


Figure 4:

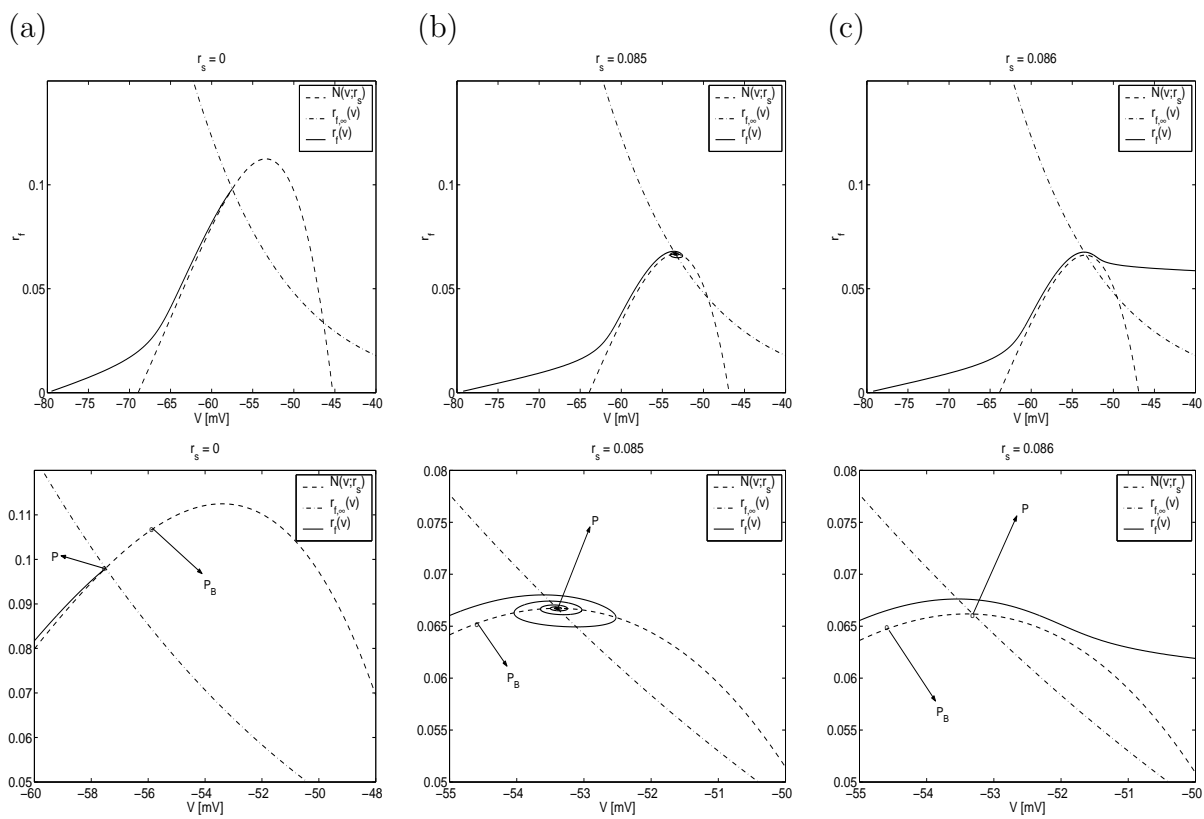


Figure 5:

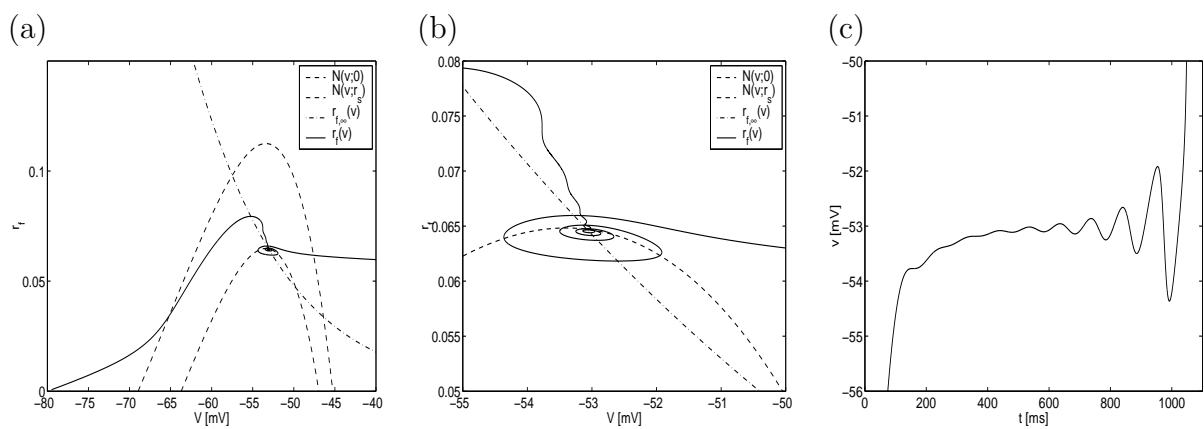


Figure 6:

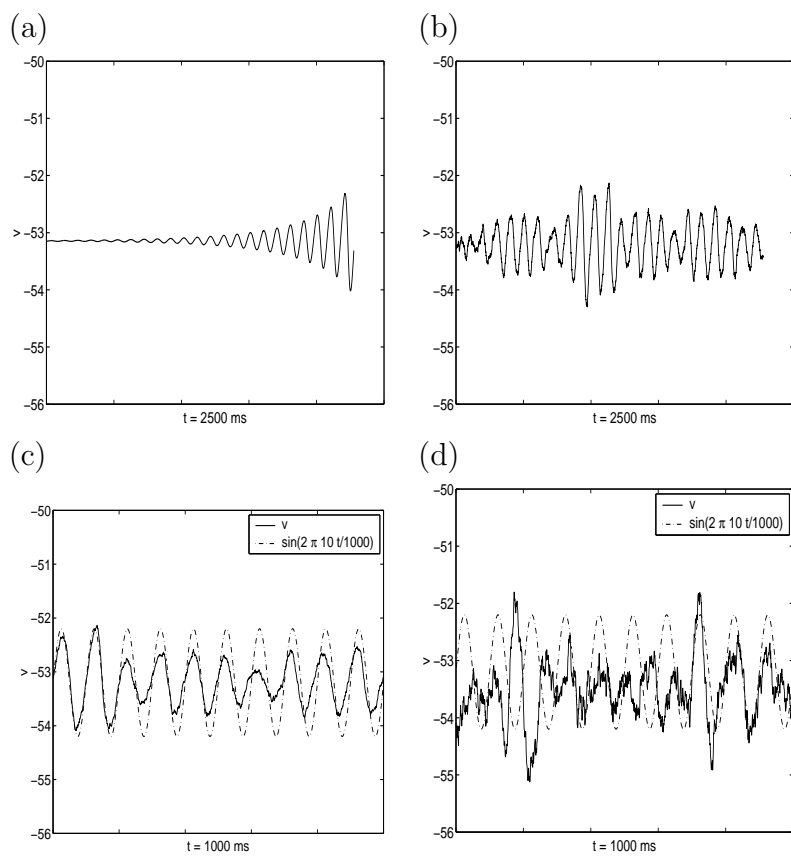


Figure 7:

Appendix A

Here we give the definitions of the functions defining $x_\infty(V)$ and $\tau_x(V)$:

$$\alpha_m(V) = -0.1(V + 23)/(e^{-0.1(V+23)} - 1),$$

$$\beta_m(V) = 4e^{-(V+48)/18},$$

$$\alpha_h(V) = 0.07e^{-(V+37)/20},$$

$$\beta_h(V) = 1/(e^{-0.1(V+7)} + 1),$$

$$\alpha_n(V) = -0.01(V + 27)/(e^{-0.1(V+27)} - 1),$$

$$\beta_n(V) = 0.125e^{-(V+37)/80},$$

$$\alpha_p(V) = 1/(0.15(1 + e^{-(V+38)/6.5})),$$

$$\beta_p(V) = e^{-(V+38)/6.5}/(0.15(1 + e^{-(V+38)/6.5})),$$

$$r_{f,\infty}(V) = 1/(1 + e^{(V+79.2)/9.78}),$$

$$\tau_{r_f}(V) = 0.51/(e^{(V-1.7)/10} + e^{-(V+340)/52}) + 1,$$

$$r_{s,\infty}(V) = 1/(1 + e^{(V+2.83)/15.9})^{58},$$

$$\tau_{r_s}(V) = 5.6/(e^{(V-1.7)/14} + e^{-(V+260)/43}) + 1.$$

Note that $\tau_p(V) = 0.15$ and $p_\infty(V) = 1/(1 + e^{-(V+38)/6.5})$.

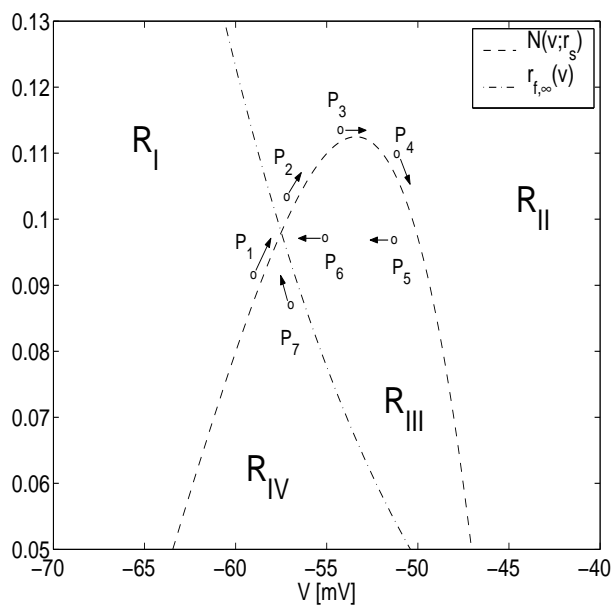


Figure 8:

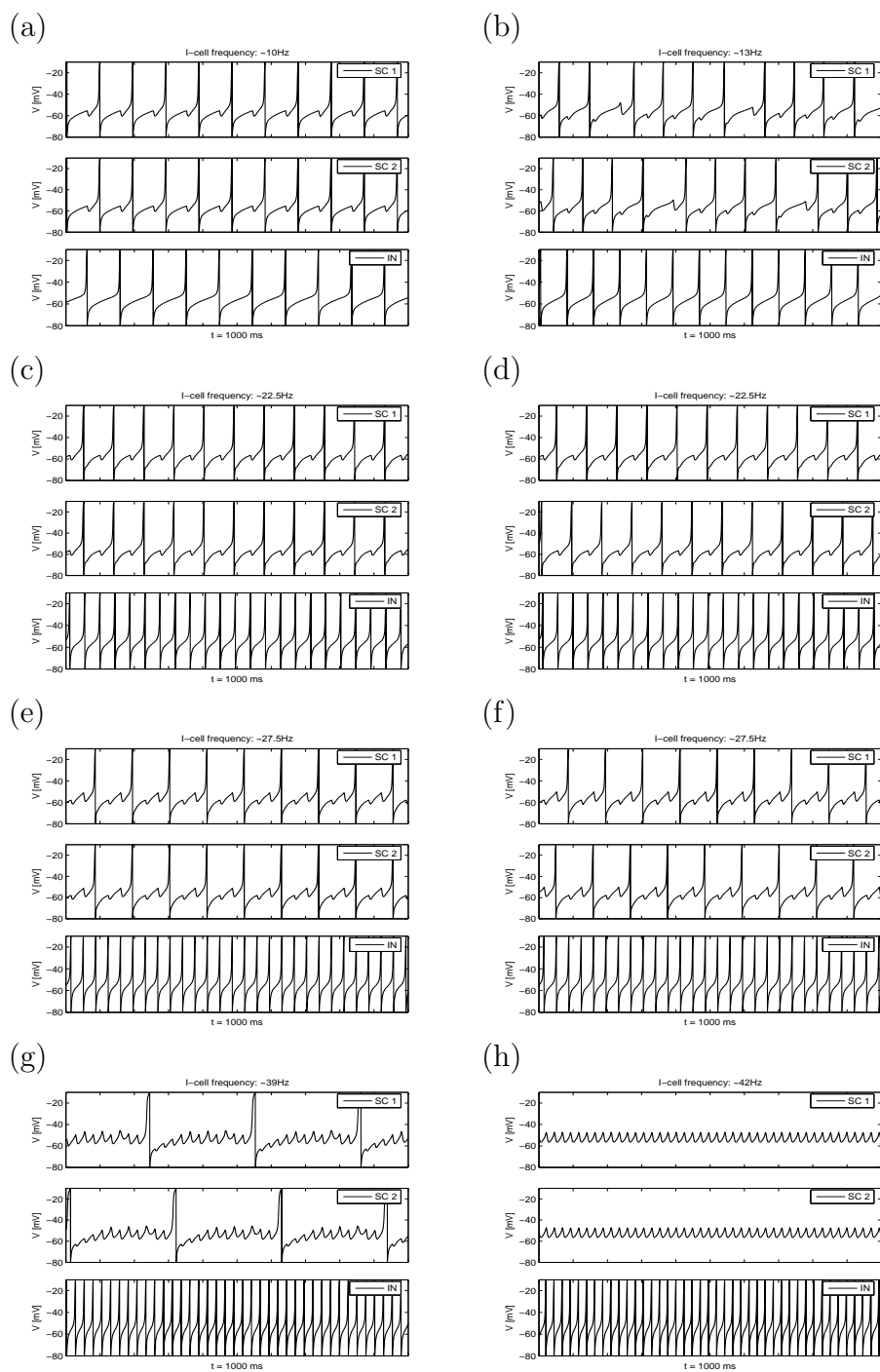


Figure 9: